

ARTICLE

Reversible Cl/Cl⁻ Redox in a Spinel Mn₃O₄ Electrode

Sean K. Sandstrom,^{#a} Qiuyao Li,^{#b} Yiming Sui,^{#a} Mason Lyons,^c Chun-Wai Chang,^c Rui Zhang,^d Heng Jiang,^a Mingliang Yu,^a David Hoang,^a William F. Stickle,^e Huolin L. Xin,^{*d} Zhenxing Feng,^{*c} De-en Jiang^{*b,f} and Xiulei Ji^{*a}

Received 00th January 20xx,
Accepted 00th January 20xx

DOI: 10.1039/x0xx00000x

A unique prospect of using halides as charge carriers is the possibility of the halides undergoing anodic redox behaviors when serving as charge carriers for the charge-neutrality compensation of electrodes. However, the anodic conversion of halides to neutral halogen species has often been irreversible at room temperature due to the emergence of diatomic halogen gaseous products. Here, we report that chloride ions can be reversibly converted to near-neutral atomic chlorine species in the Mn₃O₄ electrode at room temperature in a highly concentrated chloride-based aqueous electrolyte. Notably, the Zn²⁺ cations inserted in the first discharge and trapped in the Mn₃O₄ structure create an environment to stabilize the converted chlorine atoms within the structure. Characterization results suggest that the Cl/Cl⁻ redox is responsible for the observed large capacity, as the oxidation state of Mn barely changes upon charging. Computation results corroborate that the converted chlorine species exist as polychloride monoanions, *e.g.*, [Cl₃]⁻ and [Cl₅]⁻, inside the Zn²⁺-trapped Mn₃O₄, and the presence of polychloride species is confirmed experimentally. Our results point to the halogen plating inside electrode lattices as a new charge-storage mechanism.

Introduction

As the world continues to shift away from fossil fuels toward renewable energy sources, there is an ever-growing demand for energy-storage solutions that are safe, low-cost, and use environmentally abundant and benign material resources.¹⁻³ Unfortunately, the current Li-ion batteries are lacking in each of these considerations.^{4,5} Thus, immense efforts have been devoted to other more sustainable battery systems, *e.g.*, Na-ion,^{6,7} K-ion,^{8,9} and Zn-ion batteries.¹⁰⁻¹² Beyond these systems that operate via the reversible (de)insertion of cation charge carriers in electrode hosts, more recently, systems that use anions as the ion charge carriers have begun to attract significant interest.^{13,14} These so-called anion-shuttle batteries, including dual-ion batteries¹⁵ and anion rocking-chair batteries^{16,17}, are attractive due to their potentially high energy densities and low costs, as well as resource availability.

A unique feature of using anionic charge carriers is the possibility of the anions undergoing anodic reactions to form

neutral species, which can be deemed as plating of non-metals. Redox of Cl⁻, for example, has been studied and utilized in batteries since the 19th century.¹⁸ However, the Cl₂/Cl⁻ redox process generally suffers from poor reversibility due to loss of gaseous Cl₂.¹⁹⁻²⁵ Recently, Dai *et al.* demonstrated Cl₂||alkali metal batteries that operate via the reversible Cl₂/Cl⁻ redox at carbon-based electrodes.^{26,27} The effective trapping of Cl₂ as the charge product at the electrode hosts was deemed essential in affording the reversibility of these systems. Wang *et al.* showed high reversibility of the Cl₂/Cl⁻ redox couple in an aqueous NaCl electrolyte by storing the as-produced Cl₂ in nonaqueous, water-immiscible phases such as CCl₄.²⁸ Other approaches for overcoming the loss of gaseous Cl₂ include the formation of interhalogen species with higher boiling points, *e.g.*, BrCl and ICl, or operating the electrode below the boiling point of Cl₂ liquid.²⁹⁻³³

Another approach for avoiding the escape of gaseous Cl₂, which has yet to be explored, would be to “plate” neutral Cl atoms inside a host material. Such a mechanism would require a host material to effectively anchor the plated Cl atoms, where the strong binding between the inserted Cl and the host inhibits the formation of the Cl-Cl diatomic bond. Our group recently reported on the reversible anodic charge-storage behaviors of a spinel Mn₃O₄ electrode after trapping Zn²⁺ cations in the first discharge in a concentrated ZnCl₂-based electrolyte.³⁴ After Zn²⁺ is trapped, the as-formed Zn_{0.25}Mn₃O₄ electrode exhibited a specific charge capacity of over 200 mAh/g with an average operating potential above 1.6 V vs Zn²⁺/Zn. Herein, we report that the large capacity observed in the charging process is not due to the oxidation of Mn-ions of Mn₃O₄, where the oxidation state of Mn remains nearly unchanged during cycling, but from

^a Department of Chemistry, Oregon State University, Corvallis, OR, 97331, USA. *E-mail:* david.ji@oregonstate.edu

^b Interdisciplinary Materials Science Program, Vanderbilt University, Nashville, TN, 37235, USA. *E-mail:* de-en.jiang@vanderbilt.edu

^c School of Chemical, Biological, and Environmental Engineering, Corvallis, OR, 97331, USA. *E-mail:* zhenxing.feng@oregonstate.edu

^d Department of Physics and Astronomy, University of California, Irvine, CA, 92697, USA. *E-mail:* huolin.xin@uci.edu

^e Hewlett-Packard Co., Corvallis, OR, 97330, USA.

^f Department of Chemical and Biomolecular Engineering, Vanderbilt University, Nashville, TN, 37235, USA.

† Electronic Supplementary Information (ESI) available: [details of any supplementary information available should be included here]. See DOI: 10.1039/x0xx00000x

These authors contributed equally to this work.

a conversion from chloride to partially charged polychloride species stored in the lattice of the Mn_3O_4 cathode.

Results and discussion

Electrochemical performance of the Mn_3O_4 electrode

The electrochemical performance of the Mn_3O_4 (space group, I41/amd, PDF # 24-0734, Fig. S1)^{34,35} electrode was first evaluated using a concentrated aqueous water-in-salt electrolyte (WiSE) of 20 m ZnCl_2 + 5 m NH_4Cl . As reported before, when cycled in a two-electrode cell with Zn metal as the counter and reference electrode, the Mn_3O_4 electrode demonstrates a relatively small first discharge capacity of 128 mAh/g at a potential of ~0.6 V (vs Zn^{2+}/Zn and hereafter) and a current rate of 50 mA/g (Fig. 1a).³⁴ The subsequent charging process results in a substantially larger capacity of 218 mAh/g at an average potential of 1.66 V (the potential at half the capacity). This exceedingly large overpotential in the first cycle suggests that the initial insertion of Zn^{2+} cations is largely irreversible and that the oxidative insertion of anions was deemed responsible for most of the charging capacity. The large potential hysteresis disappears after the first cycle, and the second discharge delivers a capacity of 226 mAh/g at a slightly smaller potential than the charging process, thereby indicating the excellent reversibility of the anion-hosting reaction. A self-discharge test was performed after the first cycle to assess the stability and reversibility of the charged electrode. After idling the charged electrode for 12 hours, the electrode delivered a Coulombic efficiency of 94.3%, suggesting the good stability and reversibility of the charge products in the electrode (Fig. S2). Note that the first charge capacity with Zn^{2+} trapped is much larger than the case when we charged the Mn_3O_4

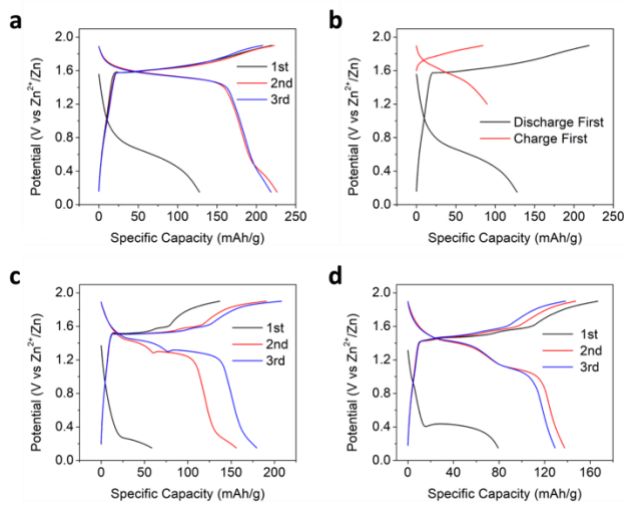


Fig. 1. **a**, Galvanostatic charge-discharge (GCD) potential profiles of the Mn_3O_4 electrode in the 20 m ZnCl_2 + 5 m NH_4Cl WiSE. **b**, Comparison of the first cycle GCD profiles of the Mn_3O_4 electrode in the WiSE when it is discharged first to a lower cutoff potential of 0.2 V and when it is charged first with the lower cutoff potential raised to 1.2 V to eliminate Zn^{2+} insertion. GCD profiles of the Mn_3O_4 electrode in common aqueous Zn-ion electrolytes of **c**, 2 M ZnSO_4 and **d**, 2 M $\text{Zn}(\text{ClO}_4)_2$.

cathode directly with a capacity of 84 mAh/g (Fig. 1b and Fig. S3). To further evaluate the effect of the initial Zn^{2+} -trapping process, we cycled the Mn_3O_4 electrode against an activated carbon counter electrode with another high-concentration chloride-based aqueous electrolyte of 15 m tetraethylammonium chloride (TEACl) (Fig. S4). The initial discharge capacity was only ~13 mAh/g, indicating that the bulky tetraethylammonium cation was not inserted into the Mn_3O_4 to any meaningful extent. The subsequent charge capacity was ~64 mAh/g, which is closer to when we charged the pristine Mn_3O_4 electrode first in the 20 m ZnCl_2 + 5 m NH_4Cl WiSE. This significant capacity difference suggests that the initial trapping of Zn^{2+} cations transforms the Mn_3O_4 structure in such a way that it facilitates the anodic process of anion storage. The question is: Can the trapped Zn^{2+} ions promote the storage of other anions?

We also investigated the redox behaviors of the Mn_3O_4 electrode in common aqueous Zn-ion electrolytes of 2 M ZnSO_4 and 2 M $\text{Zn}(\text{ClO}_4)_2$. In both electrolytes, the Mn_3O_4 electrode also exhibits a low-potential plateau around 0.4 V in the first discharge. However, the Mn_3O_4 electrode showed two apparent charge plateaus in these electrolytes, with the first plateau at potentials well below 1.66 V, the potential in the chloride-based WiSE (Figs. 1c and 1d). This two-plateau behavior is commonly observed for manganese oxide cathodes in mildly acidic aqueous electrolytes and is often attributed to H^+ and Zn^{2+} coinsertion^{36,37} or a combination of Zn^{2+} (de)insertion and $\text{MnO}_x/\text{Mn}^{2+}$ dissolution/deposition reactions.³⁸ The distinctly different redox behaviors of the Mn_3O_4 electrode in the chloride-based electrolyte and the non-chloride electrolytes are also displayed in the cyclic voltammetry (CV) curves, where Mn_3O_4 exhibits two distinct pairs of redox peaks in the 2 M ZnSO_4 in contrast to one pair in the chloride WiSE (Fig. S5). We conducted inductively coupled plasma optical emission spectroscopy (ICP-OES) after the second discharge, where the dissolved concentration of Mn in the ZnSO_4 electrolyte corresponds to 3.6 times the observed discharge capacity. However, in the ZnCl_2 WiSE electrolyte, the dissolution of Mn could only account for 4.3% of the observed discharge capacity. The results suggest that the operation of Mn_3O_4 in dilute electrolytes such as 2 M ZnSO_4 occurs by the dissolution of Mn-ions and deposition of manganese oxides, where the Zn-trapping and the associated promoted anion storage are irrelevant.

Characterization of the operation of the Mn_3O_4 electrode in the ZnCl_2 -based WiSE electrolyte

Ex situ X-ray diffraction (XRD) results indicate significant amorphization of the Mn_3O_4 structure after the initial Zn^{2+} insertion (Fig. S6). This loss in the long-range order could explain how the relatively large Cl^-/Cl anions/atoms are able to be lodged within the compact structure after the following charge. The energy dispersive X-ray spectroscopy (EDS) elemental mapping associated with TEM confirms the Zn^{2+} insertion inside the structure of Mn_3O_4 after the initial discharge (Fig. 2a). Interestingly, the Zn content appears to be particularly enriched towards the surface of the Mn_3O_4 particle. Indeed, the high-angle annular dark field scanning transmission electron microscopy (HAADF-STEM) images indicate that the surface of the Mn_3O_4 particle is furnished with Zn^{2+} cations rather than O^{2-} anions after discharging (Fig. 2b). Elemental mapping obtained after

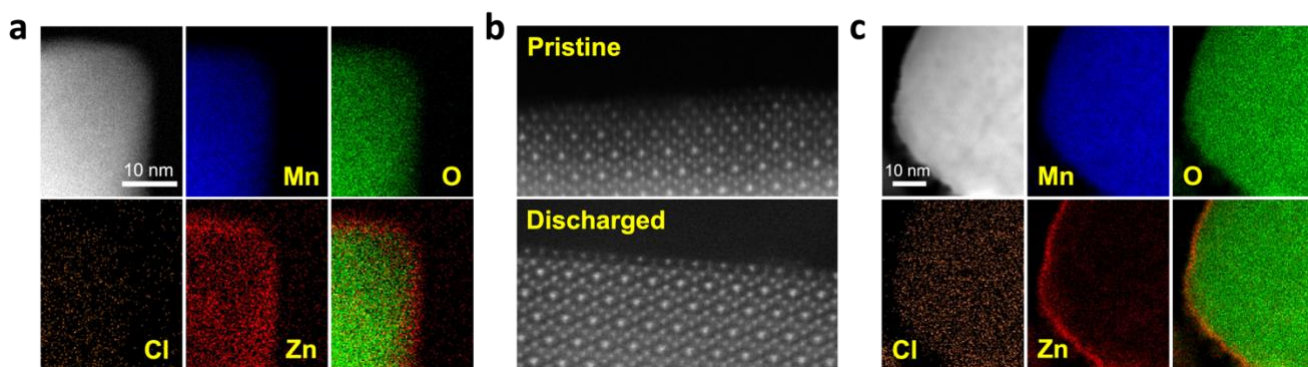


Fig. 2. **a**, An HAADF-STEM image of the Mn_3O_4 electrode and associated elemental mappings of the Mn, O, Cl, and Zn contents after the first discharge. **b**, HAADF-STEM images of the surface of the Mn_3O_4 before and after the first discharge, where the surface of the Mn_3O_4 is furnished with Zn-ions after the first discharge. **c**, HAADF-STEM image of the Mn_3O_4 electrode and associated elemental mappings of the Mn, O, Cl, and Zn contents after the first charge.

the subsequent charging process shows a uniform increase in Cl content, thereby indicating the insertion of Cl^-/Cl anions/atoms (Fig. 2c). Of note, the Zn content is significantly enriched at the Mn_3O_4 surface after the charging process, as shown by the EDS mapping and the associated line scanning profile, which indicates that the inserted Zn^{2+} cations become trapped towards the surface of the particle (Fig. 2c and Fig. S7) and the trapped Zn^{2+} cations are not static during cycling.

To reveal the charge storage mechanism of the Mn_3O_4 electrode in the chloride-based WiSE, we examined the Mn oxidation state at different state of charge (SoC) using *ex situ* synchrotron-based X-ray absorption spectroscopy (XAS).³⁹⁻⁴¹ The Mn K-edge X-ray absorption near-edge structure (XANES) studies showed slight changes in the edge positions from the pristine, to the discharged, and charged samples (Fig. 3a and Fig. S8). From fully discharged to fully charged in the first cycle, the valence state of Mn was calculated to increase by +0.09 (from $\text{Mn}^{2.83+}$ to $\text{Mn}^{2.92+}$). In theory, such an oxidation state change would result in a small specific capacity of only 31.6 mAh/g. However, we obtained a much larger specific capacity of 218 mAh/g for the first charge of the Mn_3O_4 electrode (Fig. 1a). These very subtle changes in the oxidation state of Mn were corroborated by X-ray

photoelectron spectroscopy (XPS), where the calculated oxidation states of Mn in the spectra of the pristine and charged electrodes were +2.63 and +2.75, respectively (Fig. 3b). Moreover, there were no obvious differences in the soft XAS (sXAS) spectra of Mn between the pristine, discharged, and charged samples (Fig. 3c), further indicating the lack of significant Mn redox involved in the charge storage mechanism of the Mn_3O_4 electrode in the chloride WiSE. This absence of the Mn redox in the (dis)charge processes of the Mn_3O_4 electrode supports the possibility of Cl/Cl^- redox as being the major contributor to the observed capacity because only Cl^- and water can be oxidized in the charging process other than Mn, where Cl^- should be oxidized before water due to its lower redox potential at such a high Cl^- concentration.

Effect of Zn^{2+} -trapping on Cl/Cl^- plating/stripping and the generation of polychloride anions

To gain a theoretical understanding of how the initial Zn^{2+} -trapping process facilitates the subsequent Cl^-/Cl hosting and redox reaction, we conducted density functional theory (DFT) calculations to investigate the behavior of Cl insertion in Mn_3O_4 before and after Zn

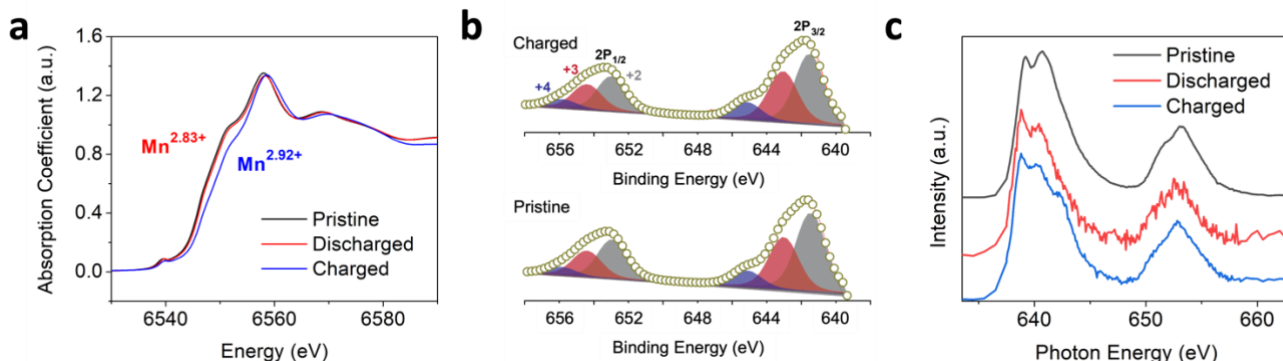


Fig. 3. **a**, Normalized XANES of the Mn K-edge spectra of the pristine Mn_3O_4 electrode and the Mn_3O_4 electrode after the initial discharge and charge. The calculated oxidation state changes from +2.83 to +2.92 from the fully discharged to the fully charged state of the Mn_3O_4 electrode in the first cycle. **b**, XPS spectra of the charged (upper) and pristine (lower) Mn_3O_4 electrode with Mn 2p_{3/2} and Mn 2p_{1/2} profiles. **c**, Mn L-edge sXAS spectra of the pristine, discharged, and charged Mn_3O_4 electrodes.

trapping. Fig. 4a and b exhibit the configurations with Zn inserted into the octahedral (Oh) site (denoted as ZnOh) and the tetrahedral (Td) site (denoted as ZnTd) of Mn_3O_4 , respectively. We found that the Td site is slightly more energetically favorable by 0.12 eV than the Oh site for Zn. During geometry optimization, the Mn atoms adjacent to Zn spontaneously move from the Td sites to Oh sites, leading to the formation of a layer of Td-site vacancies, resulting in a characteristic of spinel-to-layered structure transformation. This structural transformation results in a deformation of the crystal structure, accompanied by a volume expansion of approximately 4%. The calculated insertion energy of Zn into Mn_3O_4 is -1.0 eV (Table S1), suggesting the stability of the structure after the initial Zn-trapping process.

Subsequently, we studied the behavior of Cl insertion in Mn_3O_4 following the initial Zn-trapping process. Interestingly, upon comparing the energetics of various potential Cl intercalation sites, the computation results suggest the formation of polychloride monoanions within the structures. Specifically, within the ZnOh model, the inserted Cl atoms form trichloride $[\text{Cl}_3]^-$ anions, while within the ZnTd model, they formed T-shaped pentachloride $[\text{Cl}_5]^-$ anions (Fig. 4d, e, and Fig. S9).⁴²⁻⁴⁷ This unique finding sheds light on a new mechanism of Cl storage. The presence of these polychloride species helps explain the stability of “plated” chlorine species within the crystal structure at room temperature. Notably, the oxidation of chloride into polychlorides has been demonstrated to be thermodynamically favorable in highly concentrated acidic chloride.⁴⁷ In our work, the WiSE electrolyte used is both highly acidic and features a high chloride concentration, making the oxidation of chloride into polychloride anions feasible. In contrast, for the pristine Mn_3O_4 structure without Zn-trapping, only a small amount of dichlorides (Cl_2) was formed after the insertion of Cl atoms (Fig. S9c).

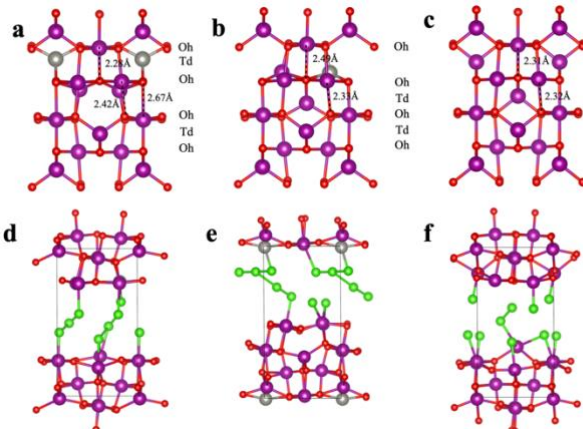


Fig. 4. The optimized structure of Zn trapped in the **a**, octahedral site (ZnOh) and **b**, tetrahedral site (ZnTd) in Mn_3O_4 . During the atomic relaxation process, Mn atoms adjacent to the Zn atom undergo spontaneous movement from the Td sites to the Oh sites, forming a layer of Td vacancies. **c**, the structure of pristine Mn_3O_4 . Optimized structure upon Cl insertion of **d**, ZnOh, **e**, ZnTd, and **f**, pristine Mn_3O_4 models. The stoichiometry is $\text{Zn}_{0.25}\text{Mn}_3\text{O}_4\text{Cl}_{1.75}$ for the Zn-trapped models and $\text{Mn}_3\text{O}_4\text{Cl}_{1.75}$ for the pristine Mn_3O_4 model.

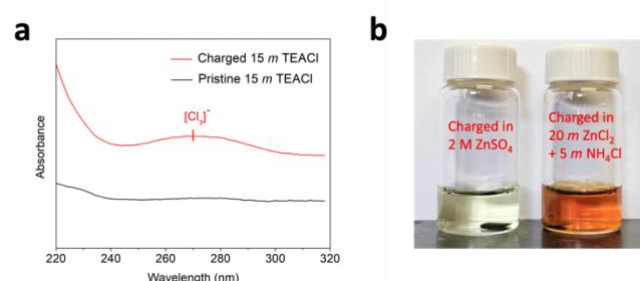


Fig. 5. **a**, UV-vis spectra of the pristine 15 m TEACl electrolyte and the 15 m TEACl electrolyte the Mn_3O_4 electrode is charged in this electrolyte. **b**, The 0.5 M KI solutions after immersing the Zn^{2+} -trapped Mn_3O_4 electrode after charging in the 2 M ZnSO_4 electrolyte (left) and after charging in the 20 m $\text{ZnCl}_2 + 5$ m NH_4Cl WiSE (right).

This finding provides an explanation for the considerably lower capacity observed in the pristine Mn_3O_4 electrode (Fig. 1b) in comparison to the Zn-trapped electrode. Furthermore, all three crystal structures experience significant volume expansion exceeding 40% upon Cl insertion. This substantial volume expansion may contribute to the observed amorphization in the *ex situ* XRD patterns after cycling the electrode (Fig. S6).

In order to assess the impact of the initial Zn-trapping on the Cl insertion process, we calculated the Cl insertion energy. Remarkably, the Cl insertion energies for the Zn-trapped models were found to be much lower compared to the pristine Mn_3O_4 model (1.9, 2.0, and 4.0 eV for the ZnOh, ZnTd, and Mn_3O_4 models, respectively). This observation indicates that the initial Zn-trapping process plays a crucial role in facilitating the oxidation of Cl^- ions and the formation/insertion of polychloride ions, thus resulting in an enhancement in Cl storage capacity.

In addition, the hosting of these polychloride anions may explain the slight oxidation of Mn observed in the XAS and XPS spectra of the charged electrode. While the majority of the observed capacity can be attributed to the redox of the inserted Cl^- species, a slight oxidation of Mn occurs to accommodate the negatively charged polychloride monoanions (Fig. 3a-c). This observation of slight oxidation in Mn aligns with the findings from the Bader charge analysis,⁴⁸ where a slight increase in the Bader charge of Mn is observed after Cl insertion (Table S2). Moreover, the COHP (crystal orbital Hamilton population) analysis⁴⁹ reveals the contribution of antibonding states near the Fermi level to the Mn-Cl bonds in the ZnOh and ZnTd models in contrast to the pristine Mn_3O_4 model. This demonstrates that the chemical bonding between Mn and Cl is weaker in the Zn-trapped models, suggesting a facile extraction of Cl^- species after Zn^{2+} -trapping (Fig. S11).

To confirm the formation and hosting of the polychloride monoanions predicted by the calculations, we conducted ultraviolet-visible (UV-vis) spectroscopy on the electrolyte after the charging process. Surprisingly, there was no noticeable difference between the spectra of the 20 m $\text{ZnCl}_2 + 5$ m NH_4Cl WiSE before and after charging the Mn_3O_4 electrode. This may be due to the strong binding between the polychloride monoanions and the host structure, considering the excellent self-discharge performance. Another

explanation is that any diffused-out polychloride would have reacted with the Zn metal counter electrode before being detected by the UV-vis measurement of the electrolyte.⁵⁰ To address the issue, we conducted the UV-vis on another highly concentrated chloride-based aqueous electrolyte of 15 *m* TEACl before and after charging the Mn₃O₄ electrode with an activated carbon free-standing film as the counter electrode (Fig. 5a). After charging, a broad peak appeared at ~270 nm by the electrolyte, which is very likely indicative of the [Cl₃]⁻ anion.^{51,52} To further confirm the existence of the polychloride monoanions formed with the Mn₃O₄ structure after charging in the 20 *m* ZnCl₂ + 5 *m* NH₄Cl WiSE, we immersed the fully charged Mn₃O₄ electrode in an aqueous solution of 0.5 M KI. It was observed that the color of the KI solution quickly turned brownish, thereby indicating the presence of the polychloride monoanion as the charge products with the Mn₃O₄ host (Fig. 5b). In stark contrast, when the Mn₃O₄ electrode charged in the 2 M ZnSO₄ electrolyte was immersed in the KI solution, the color of the solution did not change.

Conclusions

In summary, we have demonstrated and characterized a new charge storage mechanism of reversible Cl/Cl⁻ “plating/stripping” at a spinel Mn₃O₄ electrode in a high-concentration chloride-based aqueous electrolyte. The initial irreversible insertion of Zn²⁺ cations transforms the Mn₃O₄ structure in such a way that it helps facilitate the subsequent reversible Cl/Cl⁻ redox reactions. The Mn₃O₄ host acts as a “semi-catalyst” that allows the oxidation of Cl⁻ to Cl but not to Cl₂. Characterization by EDS, XAS, and XPS spectroscopies confirms that Mn redox is not responsible for most of the observed capacity. Instead, computation and experimental results suggest that the oxidized Cl⁻ anions preferentially form polychloride monoanions when hosted within the Zn²⁺-trapped Mn₃O₄. Our results present a new strategy to use semi-catalysts as electrode materials that can effectively facilitate reversible Cl/Cl⁻ “plating/stripping” reactions at room temperature.

Experimental

Chemicals and materials

Nanoscale Hausmannite Mn₃O₄ powder was synthesized by a room-temperature precipitation method.^{34,35} To begin, 1.126 g of MnSO₄·H₂O (Alfa Aesar) was dissolved into 150 mL of deionized (DI) water. The aqueous MnSO₄ solution was then titrated with 29% NH₄OH solution via dropwise additions under magnetic stirring until it reached a pH of 11. Once the solution was at pH 11, it was left to react under magnetic stirring for 1 h before being stored overnight at room temperature. The brown precipitate was then washed with DI water and centrifuged until a pH of 7 was obtained. Lastly, the precipitate was dried at 80 °C overnight to obtain the final Mn₃O₄ powder.

For the preparation of the 20 *m* ZnCl₂ + 5 *m* NH₄Cl WiSE, anhydrous zinc chloride (metals basis, 99.95%) was purchased from Thermo Scientific. Ammonium chloride (ACS, 99.5%) and the water (HPLC grade) were purchased from Alfa Aesar.

Electrochemical measurements

Electrochemical tests were done using Swagelok cells. The Mn₃O₄ working electrodes were composed of 70 wt% active mass, 20 wt% KetjenBlack, and 10 wt% polyvinylidene fluoride binder coated on carbon fiber paper current collectors. The typical active mass loading was ~2 mg/cm². The Mn₃O₄ free-standing film electrodes used for obtaining the *ex situ* XRD patterns, self-discharge experiments, and the KI solution immersion tests were composed of 70 wt% active mass, 20 wt% KetjenBlack, and 10 wt% polytetrafluoroethylene (PTFE) binder. GCD measurements were obtained using a LANDT Battery Test System CT3002A, and CV tests were conducted with a VMP-3 multi-channel workstation.

Materials characterization

XRD patterns were obtained using a Rigaku Ultima IV Diffractometer with Cu K α radiation ($\lambda=1.5406$ Å) at a scan rate of 1 degree per minute. TEM data were recorded on an aberration-corrected (scanning/) transmission electron microscope operated at 300 keV with a cold field-emission source (JEM-ARM300F Grand ARM). The energy dispersive X-ray spectroscopic (EDS) data were taken with dual 100 mm² silicon drift detectors (SDD). Hard XAS was performed at the Advanced Photon Source 10-BM in transmission mode. XAS data was processed using Athena for pre-edge background subtraction and normalization. The Mn oxidation state was determined with XANES edge position at a normalized absorbance of 0.5 and linearly interpolated with Mn₃O₄ and Mn₂O₃ standards as +2.67 (6544.8 eV) and +3 (6548.7 eV) oxidation states, respectively. sXAS at Mn L-edge was performed using total electron yield (TEY) mode at beamline 7.3.1 of Advanced Light Source (ALS) of Lawrence Berkeley National Laboratory (LBNL).

For XPS, a Physical Electronics Quantera II Hybrid was used for the analysis. The system energy scale was calibrated to Cu 2p3/2 at 932.6 eV and Au 4f at 84.0 eV. The base pressure of the system was 3×10^{-7} Pa. The XPS experiments were measured on as-loaded samples at room temperature. XPS was performed using monochromatized Al K α radiation ($h\nu = 1486.6$ eV, at 50 watts and 100 μ m beam diameter). The electron analyzer pass energy was set to 69 eV, with an emission angle of 45°. The specimens were neutralized using a combination of an electron flood gun set to 0.6 eV at 20 μ A and an ion flood gun set to 0.1 kV. The XPS data were charge corrected to the C 1s aliphatic carbon binding energy at 284.8 eV. The XPS spectra were analyzed by fitting using CasaXPS software.

UV-vis spectroscopy analyses of the electrolytes were performed using a UV-vis-NIR spectrophotometer (PerkinElmer Lambda 750).

Theoretical calculations

DFT calculations were implemented *via* the Vienna *ab initio* simulation package (VASP).⁵³ The ion-electron interaction was depicted with the projector augmented wave (PAW) method. The electron exchange correlation was expressed by the Perdew, Burke, and Ernzerhof (PBE) functional with generalized gradient approximation (GGA).⁵⁴ The cutoff energy of the plane-

wave basis set was set to 450 eV. The Brillouin zone was sampled by (3×3×2) Gamma-centered k-point mesh. The valence electrons of Mn, Zn, O, and Cl are 3d⁵4s², 3d¹⁰4s², 2s²sp⁴, and 3s²3p⁵, respectively. The convergence threshold for structural optimization and electronic energy was set to be 0.01 eV/Å in force and 1E⁻⁵ eV, respectively. The unit cell and atomic position were allowed to relax along with structure optimization. Spin polarization was considered in all computations. The DFT + U method was employed as the correction to simulate the strongly correlated materials, including transition metals.⁵⁵ The values of U and J for Mn were set to be 4.5 and 0.5 eV, respectively.^{56,57}

In this work, the crystal structures were visualized using VESTA.⁵⁸ The atomic net charge was generated with code developed by Henkelman's group via the Bader charge analysis.⁴⁸ The crystal orbital Hamilton population (COHP) analysis was obtained using LOBSTER to analyze the chemical bond.⁴⁹

The insertion energy of Zn (ΔE_{ZI}) and the insertion energy of Cl (ΔE_{CI}) were calculated by the following equations:

$$\Delta E_{ZI} = E(\text{Bulk} + \text{Zn}) - E(\text{Bulk}) - E(\text{Zn}) \quad (1)$$

$$\Delta E_{CI} = E(\text{Bulk} + n * \text{Cl}) - E(\text{Bulk}) - n * 0.5E(\text{Cl}_2) \quad (2)$$

Where $E(\text{Bulk} + \text{Zn})$ is the total energy of the Mn₃O₄ unit cell with interstitial Zn atom and $E(\text{Bulk})$ and $E(\text{Bulk} + n * \text{Cl})$ represent the total energy of a Mn₃O₄ unit cell with or without interstitial Zn atom and that contain n interstitial Cl atoms, respectively. $E(\text{Zn})$ and $E(\text{H}_2)$ represent the energy of a Zn atom and one H₂ molecule in a vacuum, respectively.

According to previous studies, the magnetic ordering of the Mn₃O₄ unit cell was set to be (↑↑↓↓↑↑).⁵⁹

Author Contributions

S.K. Sandstrom: investigation, formal analysis, visualization, data curation, writing – original draft. Q. Li: investigation, formal analysis, visualization, data curation. M. Lyons: Investigation, formal analysis, data curation. C.-W. Chang: investigation, formal analysis, data curation. R. Zhang: investigation, formal analysis, data curation. Y. Sui: investigation, formal analysis, data curation. H. Jiang: investigation. M. Yu: investigation. D. Hoang: investigation. W. F. Stickle: investigation, formal analysis, data curation. H. L. Xin: funding acquisition, writing – review and editing, supervision. Z. Feng: funding acquisition, writing – review and editing, supervision. D. Jiang: funding acquisition, writing – review and editing, supervision. X. Ji: conceptualization, funding acquisition, writing – review and editing, supervision.

Conflicts of interest

There are no conflicts to declare.

Acknowledgements

X. J. and D. J. thank the U.S. National Science Foundation (NSF) for the financial support with the Awards DMR 2221645 and DMR 2221646.

M.L., C.-W. C. and Z. F. thank the U.S. NSF for financial support from CBET 2016192 and CBET 1949870. The hard XAS measurements were done at beamline 10-BM of The Materials Research Collaborative Access Team (MRCAT) at the Advanced Photon Source. MRCAT operations are supported by the Department of Energy (DOE) and the MRCAT member institutions. This research used resources of the Advanced Photon Source; a U.S. DOE Office of Science User Facility operated for the DOE Office of Science by Argonne National Laboratory under Contract No. DE-AC02-06CH11357. The soft X-ray absorption spectroscopy measurements were performed at beamline 6.3.1 of Advanced Light Source, which is an Office of Science User Facility operated for the U.S. DOE Office of Science by Lawrence Berkeley National Laboratory and supported by the DOE under Contract No. DEAC02-05CH11231. The UCI experiments were supported by the Office of Basic Energy Sciences of the U.S. Department of Energy, under award no. DE-SC0021204. R. Z.'s effort on this project was supported by HLX's startup funding. The authors thank Jesse M. Muratli and the Keck Collaboratory for Plasma Spectrometry at Oregon State University for ICP-OES measurements.

Notes and references

1. J. Song, K. Xu, N. Liu, D. Reed and X. Li, *Materials Today*, 2021, **45**, 191-212.
2. C. Bauer, S. Burkhardt, N. P. Dasgupta, L. A.-W. Ellingsen, L. L. Gaines, H. Hao, R. Hischier, L. Hu, Y. Huang, J. Janek, C. Liang, H. Li, J. Li, Y. Li, Y.-C. Lu, W. Luo, L. F. Nazar, E. A. Olivetti, J. F. Peters, J. L. M. Rupp, M. Weil, J. F. Whitacre and S. Xu, *Nature Sustainability*, 2022, **5**, 3, 176-178.
3. J. B. Goodenough and Y. Kim, *Chemistry of Materials*, 2010, **22**, 587-603.
4. K. Turcheniuk, D. Bondarev, V. Singhal and G. Yushin, *Nature*, 2018, 467-470.
5. W. Tahil, *Implications of Future PHEV Production for Lithium Demand. Martainville: Meridian International Research*, 2007.
6. S. Y. Hong, Y. Kim, Y. Park, A. Choi, N.-S. Choi and K. T. Lee, *Energy & Environmental Science*, 2013, **6**, 7, 2067-2081.
7. Q. Li, Q. Wei, W. Zuo, L. Huang, W. Luo, Q. An, V. O. Pelenovich, L. Ma and Q. Zhang, *Chemical Science*, 2017, **8**, 1, 160-164.
8. W. Zhang, Y. Liu and Z. Guo, *Science advances*, 2019, **5**, 5, eaav7412.
9. J. Mao, C. Wang, Y. Lyu, R. Zhang, Y. Wang, S. Liu, Z. Wang, S. Zhang and Z. Guo, *Journal of Materials Chemistry A*, 2022, **10**, 37, 19090-19106.
10. L. Cao, D. Li, T. Pollard, T. Deng, B. Zhang, C. Yang, L. Chen, J. Vatamanu, E. Hu, M. J. Hourwitz, L. Ma, M. Ding, Q. Li, S. Hou, K. Gaskell, J. T. Fourkas, X.-Q. Yang, K. Xu, O. Borodin and C. Wang, *Nature Nanotechnology*, 2021, **16**, 8, 902-910.
11. D. Dong, T. Wang, Y. Sun, J. Fan and Y.-C. Lu, *Nature Sustainability*, 2023, 1-11.
12. D. Zhao, X. Pu, S. Tang, M. Ding, Y. Zeng, Y. Cao and Z. Cheng, *Chemical Science*, 2023, **14**, 30, 8206-8213.
13. S. K. Sandstrom, X. Chen and X. Ji, *Carbon Energy*, 2021, **3**, 4, 627-653.

14 Q. Liu, Y. Wang, X. Yang, D. Zhou, X. Wang, P. Jaumaux, F. Kang, B. Li, X. Ji and G. Wang, *Chem*, 2021, **7.8**, 1993-2021.

15 F. P. McCullough, C. A. Levine and R.V. Snelgrove, *U.S. Patent No. 4,830,938*, 1989.

16 M. A. Reddy and M. Fichtner, *Journal of Materials Chemistry*, 2011, **21.43**, 17059-17062.

17 X. Zhao, S. Ren, M. Bruns and M. Fichtner, *Journal of Power Sources*, 2014, **245**, 706-711.

18 L. Winter and G. Degner, *Minute Epics of Flight*, 1933.

19 J. Jorné, J. T. Kim and D. Kralik, *Journal of Applied Electrochemistry*, 1979, **9**, 573-579.

20 D. L. Thomas and D. N. Bennion, *Journal of the Electrochemical Society*, 1989, **136.12**, 3553.

21 C. F. Holmes, *Batteries for Implantable Biomedical Devices*, 1986, 133-180.

22 J. T. Kim and J. Jorné, *Journal of the Electrochemical Society*, 1977, **124.10**, 1473.

23 J. T. Kim and J. Jorné, *Journal of the Electrochemical Society*, 1980, **127.1**, 8.

24 K. A. Klinedinst and M. J. Domeniconi, *Journal of the Electrochemical Society*, 1980, **127.3**, 539.

25 P. R. Gifford and J. B. Palmisano, *Journal of the Electrochemical Society*, 1988, **135.3**, 650.

26 G. Zhu, X. Tian, H.-C. Tai, Y.-Y. Li, J. Li, H. Sun, P. Liang, M. Angell, C.-L. Huang, C.-S. Ku, W.-H. Hung, S.-K. Jiang, Y. Meng, H. Chen, M.-C. Lin, B.-J. Hwang and H. Dai, *Nature*, 2021, **596.7873**, 525-530.

27 G. Zhu, P. Liang, C.-L. Huang, C.-C. Huang, Y.-Y. Li, S.-C. Wu, J. Li, F. Wang, X. Tian, W.-H. Huang, S.-K. Jiang, W.-H. Hung, H. Chen, M.-C. Lin, B.-J. Hwang and H. Dai, *Journal of the American Chemical Society*, 2022, **144.49**, 22505-22513.

28 S. Hou, L. Chen, X. Fan, X. Fan, X. Ji, B. Wang, C. Cui, J. Chen, C. Yang, W. Wang, C. Li and C. Wang, *Nature Communications*, 2022, **13.1**, 1281.

29 J. Xu, T. P. Pollard, C. Yang, N. K. Dandu, S. Tan, J. Zhou, J. Wang, X. He, X. Zhang, A.-M. Li, E. Hu, X.-Q. Yang, A. Ngo, O. Borodin and C. Wang, *Joule*, 2023, **7.1**, 83-94.

30 Q. Guo, K.-I. Kim, S. Li, A. M. Scida, P. Yu, S. K. Sandstrom, L. Zhang, S. Sun, H. Jiang, Q. Ni, D. Yu, M. M. Lerner, H. Xia and X. Ji, *ACS Energy Letters*, 2021, **6.2**, 459-467.

31 Y. Sui, M. Lei, M. Yu, A. Scida, S. K. Sandstrom, W. Stickle, T. D. O'Larey, D.-e. Jiang and X. Ji, *ACS Energy Letters*, 2023, **8.2**, 988-994.

32 C. Yang, J. Chen, X. Ji, T. P. Pollard, X. Lü, C.-J. Sun, S. Hou, Q. Liu, C. Liu, T. Qing, Y. Wang, O. Borodin, Y. Ren, K. Xu and C. Wang, *Nature*, 2019, **569.7755**, 245-250.

33 G. Liang, B. Liang, A. Chen, J. Zhu, Q. Li, Z. Huang, X. Li, Y. Wang, X. Wang, B. Xiong, X. Jin, S. Bai, J. Fan and C. Zhi, *Nature Communications*, 2023, **14.1**, 1856.

34 H. Jiang and X. Ji, *Carbon Energy*, 2020, **2.3**, 437-442.

35 H. Jiang, Z. Wei, L. Ma, Y. Yuan, J. J. Hong, X. Wu, D. P. Leonard, J. Holoubek, J. J. Razink, W. F. Stickle, F. Du, T. Wu, J. Lu and X. Ji, *Angewandte Chemie*, 2019, **131.16**, 5340-5345.

36 W. Sun, F. Wang, S. Hou, C. Yang, X. Fan, Z. Ma, T. Gao, F. Han, R. Hu, M. Zhu and C. Wang, *Journal of the American Chemical Society*, 2017, **139.29**, 9775-9778.

37 Y. Jin, L. Zou, L. Liu, M. H. Engelhard, R. L. Patel, Z. Nie, K. S. Han, Y. Shao, C. Wang, J. Zhu, H. Pan and J. Liu, *Advanced Materials*, 2019, **31.29**, 1900567.

38 X. Guo, J. Zhou, C. Bai, X. Li, G. Fang and S. Liang, *Materials Today Energy*, 2020, **16**, 100396.

39 M. Wang and Z. Feng, *Chemical Communications*, 2021, **57.81**, 10453-10468.

40 M. Wang and Z. Feng, *Current Opinion in Electrochemistry*, 2021, **30**, 100803.

41 M. Wang, L. Árnadóttir, Z. J. Xu and Z. Feng, *Nano-Micro Letters*, 2019, **11**, 1-18.

42 H. Keil, K. Sonnenberg, C. Müller, R. Herbst-Irmer, H. Beckers, S. Riedel and D. Stalke, *Angewandte Chemie International Edition*, 2021, **60.5**, 2569-2573.

43 F. A. Redeker, H. Beckers and S. Riedel, *Chemical Communications*, 2017, **53.96**, 12958-12961.

44 M. P. Bogaard, J. Peterson and A. D. Rae, *Acta Crystallographica Section B: Structural Crystallography and Crystal Chemistry*, 1981, **37.7**, 1357-1359.

45 R. Brückner, H. Haller, M. Ellwanger and S. Riedel, *Chemistry-A European Journal*, 2012, **18.18**, 5741-5747.

46 J. Taraba and Z. Zak, *Inorganic Chemistry*, 2003, **42.11**, 3591-3594.

47 D. Degoulange, G. Rousse and A. Grimaud, *ACS Energy Letters*, 2023, **8**, 4397-4405.

48 W. Tang, E Sanville and G. Henkelman, *Journal of Physics: Condensed Matter*, 2009, **21.8**, 084204.

49 V. L. Deringer, A. L. Tchougréeff and R. Dronskowski, *The journal of physical chemistry A*, 2011, **115.21**, 5461-5466.

50 A. Van den Bossche, E. De Witte, W. Dehaen and K. Binnemans, *Green Chemistry*, 2018, **20.14**, 3327-3338.

51 H. Sun, L. Yu, X. Jin, X. Hu and D. Wang, G. Z. Chen, *Electrochemistry Communications*, 2005, **7.7**, 685-691.

52 B. Wen, C. Yang, J. Wu, J. Liu, B. Li, J. Yang and Y. Liu, *ACS Energy Letters*, 2023, **8**, 4204-4209.

53 G. Kresse and J. Furthmüller, *Physical review B*, 1996, **54.16**, 11169.

54 J. P. Perdew, K. Burke and M. Ernzerhof, *Physical review letters*, 1996, **77.18**, 3865.

55 V. I. Anisimov, J. Zaanen and O. K. Andersen, *Physical Review B*, 1991, **44.3**, 943.

56 Y.-F. Li, S.-C. Zhu and Z.-P. Liu, *Journal of the American Chemical Society*, 2016, **138.16**, 5371-5379.

57 Y.-F. Li and Z.-P. Liu, *Journal of the American Chemical Society*, 2018, **140.5**, 1783-1792.

58 K. Momma and F. Izumi, *Journal of applied crystallography*, 2011, **44.6**, 1272-1276.

59 C. Franchini, R. Podloucky, J. Paier, M. Marsman and G. Kresse, *Physical Review B*, 2007, **75.19**, 195128.